




Effect of electron-phonon scattering on the electronic transport of Weyl semimetal WP₂Kai-Cheng Zhang ^{1,*}, Chen Shen,² Hong-Bin Zhang ^{2,†}, Yong-Feng Li ^{3,4} and Yong Liu ⁵¹*School of Physical Science and Technology, Bohai University, Jinzhou 121013, China*²*Institute of Materials Science, Technical University of Darmstadt, Alarich-Weiss-Str. 2, 64287 Darmstadt, Germany*³*School of Science, Inner Mongolia University of Science and Technology, Baotou 014010, China*⁴*Key laboratory of Integrated Exploitation of Bayan Obo Multi-Metal Resources, Inner Mongolia University of Science and Technology, Baotou 014010, China*⁵*State Key Laboratory of Metastable Materials Science & Technology and College of Science, Yanshan University, Qinhuangdao, Hebei 066004, China*

(Received 11 September 2023; revised 21 December 2023; accepted 11 January 2024; published 29 January 2024)

Although the topological properties of type-II Weyl semimetal WP₂ have been widely studied by both the experiments and the theoretical calculations, the dominant electron-phonon scattering and the effect of Fermi pockets on the electronic transport still remain elusive. In this work, we investigate the electronic transport of Weyl semimetal WP₂ by the first-principles calculations and semiclassical transport theory. The results well reproduce the resistivity from the experiments. Carriers in the Fermi pockets favor much less scattering rates. Holes are found to possess much lower scattering rates than electrons at low temperatures, while both types of carriers have close scattering rates at high temperatures. At low temperatures, the scattering rates are mainly contributed by the acoustic modes, especially the transverse acoustic mode, while the rates at high temperatures are jointly contributed by acoustic modes and low-frequency optical modes, especially $B_2^{(1)}$ and $B_1^{(2)}$. Compared to other modes, the A_1 modes are found to possess larger linewidths and exhibit significant chemical potential dependent behaviors. The low-temperature resistivity is found to increase monotonously as the chemical potential increases. Moreover, both the carrier density and the resistivity can be well tuned by applying the uniaxial or volume strains. The carrier density is enhanced under the tensile strains along the a and c axes, which leads to the decreasing resistivity. In contrast, the tensile strain along the b axis suppresses the carrier density and thus increases the resistivity. The behaviors of carrier density and resistivity can be attributed to the shift of Fermi pockets and the variation of electron-phonon coupling strength under the strains.

DOI: [10.1103/PhysRevB.109.045149](https://doi.org/10.1103/PhysRevB.109.045149)**I. INTRODUCTION**

Weyl semimetals are a kind of material whose bands host massless and chiral fermions with nontrivial topological invariants [1–3]. Due to the complex Fermi surfaces and the nontrivial Berry curvatures, Weyl semimetals are found to possess many novel transport properties [3,4]. For instance, transport phenomena, i.e., extremely large magnetoresistance [5,6], ultrahigh mobility [5,6], and the violation of Wiedemann-Franz law [7], and the planar Hall effect [8,9] have been observed in Weyl semimetals.

Recently, transition metal diphosphide WP₂ has been predicted to possess a robust phase of type-II Weyl semimetal [10,11]. Experiments have shown extremely high magnetoresistance proportional to $H^{1.8-1.9}$ in WP₂ at low temperatures, which is attributed to the chiral anomaly [12,13]. The electrical conductivity is mainly contributed by hole carriers at low temperatures, while it is dominated by electron carriers at high temperatures [12]. Moreover, an extremely large ratio of resistivity $\rho(300\text{ K})/\rho(2\text{ K})$ has been reported in WP₂ [12], indicating a large suppression of backscattering at low temperatures. It is believed that carriers undergo large-angle

scattering at high temperatures while they are mainly scattered with small angles at low temperature. Electrons flow in the semimetal like a fluid with viscosity, obeying the hydrodynamic transport [14,15]. Experiment has demonstrated the hydrodynamic signature of electrons flowing in WP₂ wires with finite widths [16]. Theoretically, the resistivity and scattering rates of WP₂ have been calculated by solving the linearized Boltzmann transport equation (BTE) with momentum relaxation time approximation [17]. It is found that the electron-phonon scattering dominates over the electron-electron scattering in the carrier transport of WP₂. Also, measurements reveal that WP₂ has the temperature-dependent anisotropy of electronic transport properties [18], which arise from the anisotropic Fermi velocity and electron-phonon scattering. Recently, anomalous phonon linewidth of the $A_1^{(1)}$ mode has been identified in WP₂ by the Raman spectroscopy [19], indicating significant electron-phonon scattering in the semimetal. One may wonder what roles the phonon modes play in carrier scattering and how the electron-phonon scattering is affected by the Fermi pockets. Motivated by this experiment [19], we want to explore the dominant phonon modes in carrier scattering as well as the effect of shifted Fermi pockets on the electronic transport.

In this article, we investigate the electronic transport properties of WP₂ by first-principles calculation plus the Ziman resistivity formula. The mode-resolved resistivity and

*kc Zhang@yeah.net

†hzhang@tmm.tu-darmstadt.de

scattering rates are evaluated to determine the dominant phonon mode in carrier scattering. We calculate the chemical potential dependent resistivity to explore the contributions of Fermi pockets to the resistivity. Also, the phonon linewidth and the electron-phonon coupling (EPC) strength with respect to the chemical potential are calculated to investigate the dependence of the electron-phonon interaction on the chemical potential. Furthermore, the dependence of resistivity on the lattice and volume deformations is investigated and the underlying scattering mechanism is discussed. The rest of the article is organized as follows. In Sec. II, we introduce the calculation methods and details. The calculation results and the discussions on the underlying physics are presented in Sec. III. Finally, a conclusion is given in Sec. IV.

II. METHODS AND CALCULATION DETAILS

A. Method of carrier transport calculation

When electrons are driven to flow in the metals by a small electric field, the conductivity tensor can be expressed as [20]

$$\alpha_{\alpha\beta} = \frac{-e}{(2\pi)^3} \sum_n \int d^3k \mathbf{v}_{n\mathbf{k}}^\alpha \partial_{E_\beta} f_{n\mathbf{k}}, \quad (1)$$

where $\mathbf{v}_{n\mathbf{k}}$ and $f_{n\mathbf{k}}$ are the band velocity and distribution function for electrons. It is noticed that the conductivity relies on the evaluation of $\partial_{E_\beta} f_{n\mathbf{k}}$. The term $\partial_{E_\beta} f_{n\mathbf{k}}$ generally includes two parts of contributions, i.e., the drift of Fermi sphere and the excitation of quasiparticles from the Fermi sphere. If we omit the quasiparticle excitation and only preserve the drift of Fermi sphere, the derivative can be approximated to $\partial_{E_\beta} f_{n\mathbf{k}} \approx e v_{n\mathbf{k}}^\beta (\partial f_{n\mathbf{k}}^0 / \partial \varepsilon_{n\mathbf{k}}) \tau_{n\mathbf{k}}$, which is valid in the small field limit. Correspondingly, the resistivity can be expressed as $\rho = m^* \langle \tau^{-1} \rangle / (n_c e^2)$, where $\langle \tau^{-1} \rangle$ is the average scattering rate $\tau_{n\mathbf{k}}^{-1}$ weighted by $\sum_n \int \frac{d^3k}{\Omega_{\text{BZ}}} (-\partial f_{n\mathbf{k}}^0 / \partial \varepsilon_{n\mathbf{k}})$. Since the electron-phonon matrix elements remain nearly constant within the range of $k_B T$ around the Fermi level, the resistivity can be expressed as the Ziman resistivity formula [21,22]

$$\rho = \frac{4\pi m^* 2k_B T}{e^2 \hbar n_c} \int_0^\infty \frac{d\omega}{\omega} \frac{[\hbar\omega / (2k_B T)]^2 \alpha_{\text{tr}}^2 F(\omega)}{\sinh^2[\hbar\omega / (2k_B T)]}. \quad (2)$$

In the above equation, the parameter n_c , usually denoted as the charge in the cell, is set to be 1.0 in the calculations. $\alpha_{\text{tr}}^2 F(\omega)$ is the transport Eliashberg function [23], which can be written as

$$\alpha_{\text{tr}}^2 F(\omega) = \frac{1}{2\hbar N(\varepsilon_F)} \sum_{mnv} \iint \frac{d^3k d^3q}{\Omega_{\text{BZ}}^2} |g_{mnv}(\mathbf{k}, \mathbf{q})|^2 \times \delta(\varepsilon_F - \varepsilon_{n\mathbf{k}}) \delta(\varepsilon_F - \varepsilon_{m\mathbf{k}+\mathbf{q}}) \delta(\omega - \omega_{\mathbf{q}v}), \quad (3)$$

where $N(\varepsilon_F)$ is the density of states at the Fermi level. The electron-phonon matrix element, $g_{mnv}(\mathbf{k}, \mathbf{q})$, can be written as [20,24]

$$g_{mnv}(\mathbf{k}, \mathbf{q}) = \sqrt{\frac{\hbar}{2M\omega_{\mathbf{q}v}}} \langle n\mathbf{k} | \frac{\partial V_{KS}}{\partial u_{\mathbf{q}v}} | m\mathbf{k} + \mathbf{q} \rangle, \quad (4)$$

which represents the hopping probability of electrons from the state $|n\mathbf{k}\rangle$ to the state $|m\mathbf{k} + \mathbf{q}\rangle$ after absorbing a phonon $|\mathbf{q}v\rangle$.

To evaluate the carrier scattering rates, we calculated the self-energy of carriers by the Fan-Migdal relation [24]:

$$\Sigma_{n\mathbf{k}}^e = \sum_{mv} \int_{\text{BZ}} \frac{d\mathbf{q}}{\Omega_{\text{BZ}}} |g_{mnv}(\mathbf{k}, \mathbf{q})|^2 \times \left[\frac{n_{\mathbf{q}v}(T) + f_{m\mathbf{k}+\mathbf{q}}(T)}{\omega - (\varepsilon_{m\mathbf{k}+\mathbf{q}} - \varepsilon_F) + \omega_{\mathbf{q}v} + i\delta} + \frac{n_{\mathbf{q}v}(T) + 1 - f_{m\mathbf{k}+\mathbf{q}}(T)}{\omega - (\varepsilon_{m\mathbf{k}+\mathbf{q}} - \varepsilon_F) - \omega_{\mathbf{q}v} + i\delta} \right]. \quad (5)$$

The k -dependent scattering rate $\gamma_{n\mathbf{k}}$ can be expressed as $\gamma_{n\mathbf{k}} = 2(\text{Im}\Sigma_{n\mathbf{k}}^e)/\hbar$. Since the carriers contributing to the conductivity are mainly distributed as $-\partial f_{n\mathbf{k}}^0 / \partial \varepsilon_{n\mathbf{k}}$, the scattering rate can be evaluated as

$$\gamma = \frac{\sum_n \int \frac{d^3k}{\Omega_{\text{BZ}}} \gamma_{n\mathbf{k}} \left(-\frac{\partial f_{n\mathbf{k}}^0}{\partial \varepsilon_{n\mathbf{k}}} \right)}{\sum_n \int \frac{d^3k}{\Omega_{\text{BZ}}} \left(-\frac{\partial f_{n\mathbf{k}}^0}{\partial \varepsilon_{n\mathbf{k}}} \right)}. \quad (6)$$

In the presence of EPC interaction, the phonon spectrum usually exhibits the finite linewidth, which can be evaluated by the imaginary part of phonon self-energy, i.e., $\Gamma_{\mathbf{q}v}^{\text{ph}} = \text{Im}(\Sigma_{\mathbf{q}v}^{\text{ph}})$. Given the phonon in the state $|\mathbf{q}v\rangle$, the self-energy can be expressed as [25]

$$\Sigma_{\mathbf{q}v}^{\text{ph}} = 2 \sum_{mn} \int_{\text{BZ}} \frac{d^3k}{\Omega_{\text{BZ}}} |g_{mnv}(\mathbf{k}, \mathbf{q})|^2 \times \frac{f_{n\mathbf{k}}(T) - f_{m\mathbf{k}+\mathbf{q}}(T)}{(\varepsilon_{m\mathbf{k}+\mathbf{q}} - \varepsilon_{n\mathbf{k}}) - \omega_{\mathbf{q}v} - i\delta}. \quad (7)$$

To evaluate the contribution of phonon modes to the resistivity, the EPC strength was calculated as [25]

$$\lambda_{\mathbf{q}v} = \frac{1}{N(\varepsilon_F) \omega_{\mathbf{q}v}} \sum_{nm} \frac{d^3k}{\Omega_{\text{BZ}}} |g_{mnv}(\mathbf{k}, \mathbf{q})|^2 \times \delta(\varepsilon_{n\mathbf{k}} - \varepsilon_F) \delta(\varepsilon_{n\mathbf{k}+\mathbf{q}} - \varepsilon_F). \quad (8)$$

In the calculations, the resistivity and the scattering rates are evaluated on very dense k and q mesh ($20 \times 20 \times 20$) by using the Wannier-Fourier interpolation technique, as implemented in the ELECTRON-PHONON WANNIER (EPW) code [25]. To do this, the electron and phonon Hamiltonian and EPC matrix elements are first calculated on the coarse k and q mesh ($4 \times 4 \times 4$). Then they are transformed from the Bloch representation into the Wannier representation by constructing maximally localized Wannier functions [26]. After that, they are transformed into the Bloch representation again by interpolating to the fine k and q mesh, through which the physical quantities are evaluated.

B. Methods of electron and phonon calculations

The electronic structure of WP_2 is studied by first-principles calculation based on the method of plane waves, as implemented in QUANTUM ESPRESSO (QE) code [27]. Optimized norm-conserving Vanderbilt (ONCV) pseudopotentials [28] of full-relativity form, together with the exchange-correlation functional of the Perdew-Burke-Ernzerhof (PBE) form [29], are obtained from the PseudoDojo [30]. The shell configurations take $4f^{14}5s^2p^6d^46s^2$ and $3s^2p^3$ for W and P

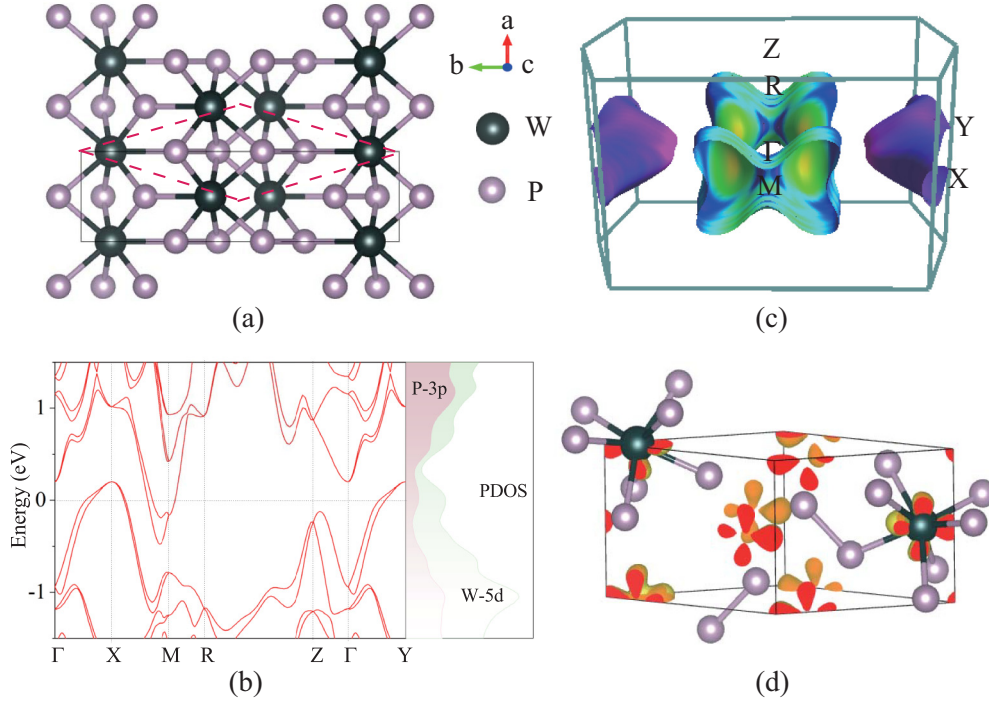


FIG. 1. (a) Crystal structure of WP_2 . The solid (dashed) lines mark the unit (primitive) cell. (b) Energy band of WP_2 along the k path in the Brillouin zone. The projected density of states are shown for W and P atoms, respectively. (c) Fermi surface with the color-mapped Fermi velocity in the Brillouin zone. The purple and green surfaces represent the hole and electron pockets, respectively. The high symmetry points are also marked in the plot. (d) Partial density of charge in the energy window of $(\epsilon_F - 0.1, \epsilon_F)$.

atoms, respectively. A k mesh of $10 \times 10 \times 10$ is used for the static calculation and the energy convergence criterion is set to be 10^{-9} Ry. The phonon dispersion is calculated by the density-functional perturbation theory (DFPT) and a q mesh of $4 \times 4 \times 4$ is used for the non-self-consistent calculations.

III. RESULTS AND DISCUSSION

A. Electronic structure and phonon dispersion

The orthorhombic phase of WP_2 possesses the space group of $Cmc2_1$ and point group of C_{2v} with one mirror plane, one glide plane, and one twofold screw axis. The conventional cell contains two Wyckoff sites occupied by 4 W and 8 P atoms, respectively. Each W atom bonds to seven nearest neighboring P atoms. Two irreducible P atoms bond to four and three nearest neighboring W atoms, respectively, while the nearest P atoms covalently bond to each other, as shown in Fig. 1(a). Bader charge analysis reveals that W loses the charge of 0.757 e , while two irreducible P atoms gain the charges of 0.435 and 0.322 e , respectively. The band structure of WP_2 has been self-consistently calculated by including spin-orbit coupling (SOC), as shown in Fig. 1(b). It is found that the Fermi pocket of electrons has been formed along the path of $X-M$, while the Fermi pocket of holes has been formed along the paths of $\Gamma-X$ and $\Gamma-Y$. The Fermi pockets possess 0.124 holes and electrons, respectively, which corresponds to the charge concentration of $1.39 \times 10^{21} \text{ cm}^{-3}$ for holes and electrons, in agreement with the experimental result ($\approx 10^{21} \text{ cm}^{-3}$) [12,18]. This means that pristine WP_2 is the semimetal with compensated carriers, similar to the Weyl semimetals WTe_2 [31] and

$MoTe_2$ [32]. Double degeneracies arise at the points of X and M with the energy of 0.19 and -0.16 eV relative to the Fermi level, respectively.

To further analyze the states near the Fermi level, we calculated the projected density of states (PDOS) for W and P atoms, respectively, as shown in Fig. 1(b). Near the Fermi level, the $5d$ states of W atoms weigh much significantly over the $3p$ states of P atoms, indicating the predominant role in the band composition. To better visualize the electronic states at the Fermi level, we calculated the Fermi surface in the Brillouin zone, as shown in Fig. 1(c). The hole pocket is located around the X and Y points with the lower Fermi velocity, while the electron pocket lies near the M point with larger Fermi velocity. The flat nature of the Fermi pockets indicates that carriers mainly flow in the ab plane, especially along the a axis. As shown in Fig. 1(d), the partial charge density within the energy window of $(\epsilon_F - 0.1, \epsilon_F)$ also shows the characteristic of $5d$ orbitals, indicating the dominant contribution to the Fermi surface from W atoms.

Figure 2(a) shows the phonon dispersion along the q path in the Brillouin zone. The phonon bands are divided into three bunches, i.e., the low-frequency bands with the frequency below 188 cm^{-1} , the medium frequency of $228-432 \text{ cm}^{-1}$, and the high frequency of $482-530 \text{ cm}^{-1}$. It is found that the acoustic modes approach zero at the point Γ . The low-frequency modes are mainly originated from the relative motions between W atoms, while the medium and high frequency modes arise from the relative motions between P atoms, as demonstrated by the projected phonon density of states in Fig. 2(b). The bunching of low-frequency modes

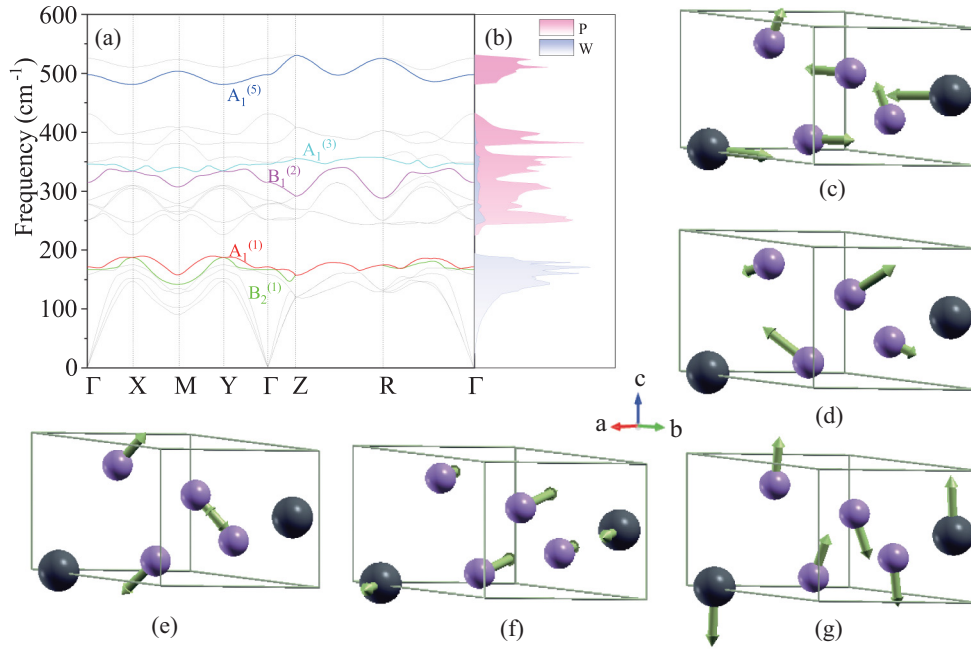


FIG. 2. (a) Phonon dispersion along the q path in the Brillouin zone. (b) Projected phonon density of states for P and W atoms. (c)–(g) Atomic displacements for the phonon modes of $A_1^{(1)}$ (c), $A_1^{(3)}$ (d), $A_1^{(5)}$ (e), $B_1^{(2)}$ (f), and $B_2^{(1)}$ (g), respectively. The numbers in the brackets represent the orders of phonon modes sequenced from the lowest optical modes in the subgroup.

along with the band gap of 40 cm^{-1} suppresses the phonon-phonon scattering between acoustic and medium-frequency optical modes.

According to the symmetry of mechanical representation, the phonon modes of WP_2 at Γ can be decomposed as

$$\Gamma = 6A_1 \oplus 3A_2 \oplus 3B_1 \oplus 6B_2 \quad (9)$$

among which three acoustic modes belong to B_1 , B_2 , and A_1 and the left ones are the optical modes with Raman activity. Except for the acoustic modes, we name the optical modes by sequencing the frequencies of the modes in their symmetry subgroups. For instance, the optical mode $A_1^{(1)}$ means that it is the optical mode with the lowest frequency in the A_1 subgroup. As listed in Table I, our calculation gives the phonon frequencies of 172.0 , 346.0 , 497.7 , 314.7 , and 168.0 cm^{-1} for the optical modes $A_1^{(1)}$, $A_1^{(3)}$, $A_1^{(5)}$, $B_1^{(2)}$, and $B_2^{(1)}$, respectively, in good agreement with the experiment results [18,19]. Compared to the A_1 modes, the calculated frequencies of B_2 modes generally show slightly larger deviation from the experimental data. As shown in Figs. 2(c)–2(g), the atomic

displacements are plotted for these optical modes, which play an important role in the carrier scattering and phonon self-energy. The vibrations of low-frequency modes $A_1^{(1)}$ and $B_2^{(1)}$ mainly come from the opposite motions between the nearest W and P atoms, while the vibrations of $A_1^{(3)}$, $A_1^{(5)}$, and $B_1^{(2)}$ originate from the relative motions between nearest neighbor P atoms. Recently, Raman spectroscopy measurement on WP_2 has revealed that the A_1 modes exhibit anomalous phonon linewidths [19], which arise from significant electron-phonon coupling. The A_1 mode corresponds to the antiparallel and parallel motions along the b and c axes, respectively, between two irreducible atoms occupied Wyckoff positions $(0, y, z)$ and $(0, -y, z + 1/2)$, as shown in Fig. 2. We will discuss their anomalous linewidths in the following sections.

B. Mode-resolved electrical resistivity and scattering rates

The temperature dependence of resistivity has been calculated by using the Ziman resistivity formula, as shown in Fig. 3(a). At 300 K, the resistivity ρ_{theory} takes $65.0 \mu\Omega \text{ cm}$, slightly above the experimental value of $52.5 \mu\Omega \text{ cm}$ [13].

TABLE I. Calculation results of optical phonon frequency ν (cm^{-1}) and phonon linewidth Γ_{ph} (meV) at $\mathbf{q} = 0$. The experimental values ν_{expt} and $\Gamma_{\text{ph}}^{\text{expt}}$.

	$A_2^{(1)}$	$B_2^{(1)}$	$A_1^{(1)}$	$A_2^{(2)}$	$B_1^{(1)}$	$A_2^{(3)}$	$A_1^{(2)}$	$B_2^{(2)}$	$B_1^{(2)}$	$A_1^{(3)}$	$B_2^{(3)}$	$A_1^{(4)}$	$B_2^{(4)}$	$A_1^{(5)}$	$B_2^{(5)}$
ν	158.9	168.0	172.0	251.7	251.7	278.1	278.1	284.5	314.7	346.0	349.5	380.8	431.5	497.7	525.6
ν_{expt}	159.2 ^a	173.3 ^b	168.4 ^a	261.0 ^b	256.3 ^a	282.2 ^a	284.1 ^a	297.9 ^b	326.2 ^b	359.9 ^a	367.0 ^c	392.4 ^a	440.0 ^c	511.7 ^a	550.0 ^c
Γ_{ph}	0.03	0.02	0.32	0.07	0.07	0.20	0.20	0.02	0.06	0.45	0.18	0.17	0.06	0.11	0.06
$\Gamma_{\text{ph}}^{\text{expt}}$	0.07 ^b	0.09 ^b	0.36 ^b	0.08 ^b	0.08 ^b	0.28 ^b	0.28 ^b	0.08 ^b	0.07 ^b	0.31 ^b	0.23 ^b	0.15 ^b	0.21 ^b	0.18 ^b	0.20 ^b

^aReference [18].

^bReference [19].

^cReference [33].

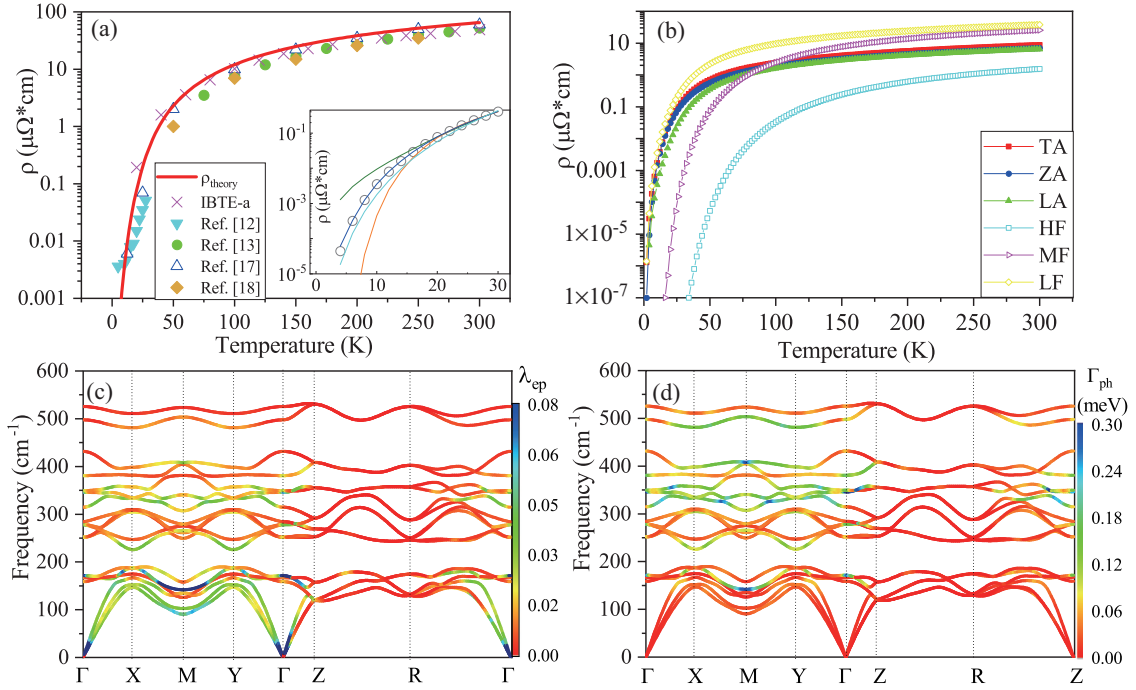


FIG. 3. (a) Temperature dependence of resistivity for WP_2 . The solid dots are the experimental data from Refs. [12], [13], and [18]. The empty triangle dots are the theoretical data from Ref. [17]. The crossing symbols represent the solution of IBTE along the a axis. The inset shows the numerical fittings of low-temperature resistivity according to the functions of $\rho = \rho_0 + aT^2 + bT^5$ (olive), $\rho = \rho_0 + ce^{-T_0/T}$ (orange), $\rho = \rho_0 + bT^5$ (cyan), and $\rho = \rho_0 + aT^2 + bT^5 + ce^{-T_0/T}$ (blue). (b) Mode-resolved resistivity as the function of temperature. Both the acoustic phonon modes of TA, ZA, and LA, and the bundles of phonon modes, i.e., low-frequency (LF), medium-frequency (MF), and high-frequency (HF) modes, are considered separately. (c) Color-mapped EPC strength along the q path. (d) Color-mapped phonon linewidth (in the unit of meV) along the q path in the Brillouin zone.

At 10 K, ρ_{theory} takes 3.6 $n\Omega\text{cm}$, close to the experimental value of 4.0 $n\Omega\text{cm}$ [12]. As the temperature approaches zero, the resistivity decays more rapidly compared to the experimental value, which remains a small value due to the impurity scattering effect. At the mediate temperatures, the calculated resistivity deviates from the experiment data. For instance, the calculated resistivity gives 6.4 $\mu\Omega\text{cm}$ at temperature 75 K, in contrast to the experiment value of 3.5 $\mu\Omega\text{cm}$ [13]. Note that the Ziman resistivity formula inversely depends on the free parameter n_c , which can be used to adjust the initial resistivity. Taking the initial ratio of resistivity $\rho_{\text{theory}}(300\text{ K})/\rho_{\text{expt}}(300\text{ K}) = 1.24$ into account, the calculated resistivity at 75 K will be renormalized to 4.3 $\mu\Omega\text{cm}$.

Similarly, the calculated ρ_{theory} takes 0.076 $\mu\Omega\text{cm}$ at 20 K, in contrast to 0.016 $\mu\Omega\text{cm}$ from the experiment [12]. Taking $\rho_{\text{expt}}(300\text{ K}) = 25.0\ \mu\Omega\text{cm}$ [12] and $\rho_{\text{theory}}(300\text{ K})/\rho_{\text{expt}}(300\text{ K}) = 2.6$ into account, the calculated resistivity will be renormalized to 0.029 $\mu\Omega\text{cm}$, closer to the experiment data. Overall, our results are close to the experiment data [12,13,18]. Moreover, our results also agree well with the theoretical data from the linearized BTE [17], indicating the validation of our method. We also calculated the resistivity by iterative Boltzmann transport equation (IBTE) with the smearing parameter $\delta = 0.01\text{ eV}$ in the electron-phonon scattering process. The result of IBTE agrees well with the experiment data at high temperatures. However, as the temperature decreases, it begins to overestimate the resistivity due to the spurious temperature arising from the finite

smearing. At low temperatures, it is very hard to achieve the convergence of IBTE.

Previously, two type of scattering mechanisms, namely, the electron-phonon and phonon drag scattering, were proposed to explain the resistivity behavior of WP_2 at low temperatures [12]. The resistivity typically favors T^2 and T^5 behaviors for electron-electron and electron-phonon scattering, respectively, while the scattering of phonon drag leads to the exponential decay of resistivity. As shown in the inset of Fig. 3(a), both the functions $\rho = \rho_0 + aT^2 + bT^5$ and $\rho = \rho_0 + ce^{-T_0/T}$ cannot well fit the resistivity at low temperatures, while the function $\rho = \rho_0 + aT^2 + bT^5 + ce^{-T_0/T}$ fits the resistivity quite well, similar to the case of Ref. [12]. However, the good fitting cannot be taken as multiple scattering mechanisms weighted equally in the transport since the latter function has more free parameters. We find that the function $\rho = \rho_0 + bT^5$ can fit the data much better than the functions $\rho = \rho_0 + aT^2 + bT^5$ and $\rho = \rho_0 + ce^{-T_0/T}$, indicating the dominant role of electron-phonon scattering in the transport. To find out the phonon modes dominating in the carrier scattering, we calculate the mode-resolved resistivity for the longitudinal acoustic mode (LA), transverse acoustic mode (TA), and flexible acoustic mode (ZA), as shown in Fig. 3(b). Moreover, the resistivity contributed by the bundles of phonon modes, i.e., low-frequency, medium-frequency, and high-frequency modes, are also calculated. Compared to the resistivity of medium-frequency and high-frequency modes, the resistivity mainly comes from the

carrier scattering of low-frequency modes. For instance, the low-frequency modes contribute to 58.3% of the resistivity at 300 K, while their contribution nearly increases to 100% at 10 K. This means that the resistivity at low temperature mainly originates from the carrier scattering of low-frequency modes.

Further, the mode-resolved resistivity of TA and ZA takes 1.82 and 1.50 $n\Omega$ cm at 10 K, respectively, which accounts for 50.6% and 41.7% of the total resistivity, while LA only contributes 7.5% of the resistivity. This means that the resistivity mainly arises from the scattering of TA and ZA modes. To further illustrate the contribution of phonon scattering to the resistivity, we calculate the EPC strength λ_{ep} along the q path in the Brillouin zone, as shown in Fig. 3(c). Generally, λ_{ep} takes small values for medium- and high-frequency modes while it has large values for low-frequency modes, especially near the Γ point, since λ_{ep} is inversely proportional to the phonon frequency. This means the acoustic modes with small q contribute heavily to the resistivity. Also, λ_{ep} has larger values along the path Γ -X-M-Y- Γ than R-Z. Because the Fermi pockets are mainly distributed along the former path, electrons can successfully be scattered to other states near the Fermi level. In other words, electrons are scattered in larger phase space along the former path, which results in larger λ_{ep} . The optical phonon mode $B_2^{(1)}$ is found to possess large λ_{ep} at M point, indicating the additional contribution to the resistivity.

In the semimetal, besides the phonon-phonon interaction, EPC interaction usually reduces the phonon lifetimes by adsorbing or emitting phonon and hence leads to the finite linewidth, as illustrated in Fig. 3(d). The phonon modes with medium and high frequency are found to have large phonon linewidth (about 0.1–0.3 meV), which is mainly distributed along the path of Γ -X-M-Y- Γ , while the low-frequency modes have small values of linewidth. The larger linewidth along the preferred path can be attributed to the larger phase space for successful electron-phonon scattering, similar to the case of λ_{ep} . The magnitude of phonon linewidth is comparable to that of the metal Al [34]. We list the calculated phonon linewidths of Γ_{ph} at $\mathbf{q} = 0$ in Table I, together with the experimental data, for all the optical modes. Overall, the A_1 modes have much larger linewidths than other modes, consistent with the experimental observation [19]. Compared to the B_2 modes, the linewidths of the A_1 modes are close to the experimental values. Due to the weak Raman intensity, the phonon linewidths of B_2 modes have much larger error bars than those of A_1 modes [19]. Therefore, larger deviation of Γ_{ph} from the experimental data can be expected for the B_2 modes.

To study the carrier scattering in WP_2 , we calculate the hole and electron scattering rates by the Fan-Migdal self-energy approximation, as shown in Fig. 4(a). We use the adaptive smearing [35] instead of the Gaussian smearing in the calculation to avoid the spurious temperature brought by the constant smearing. At 10 K, electrons have the scattering rate of 0.55 ps^{-1} , which is about twice the rate of 0.26 ps^{-1} of holes. Below 10 K, the ratio γ_e/γ_h further increases, indicating a predominant role of holes at low temperatures. In contrast, both carriers get close rates at 300 K, i.e., 59.3 and 52.4 ps^{-1} for holes and electrons, respectively. According to $\mu = e/(m^*\gamma)$, the mobility can be estimated to be 2166 and

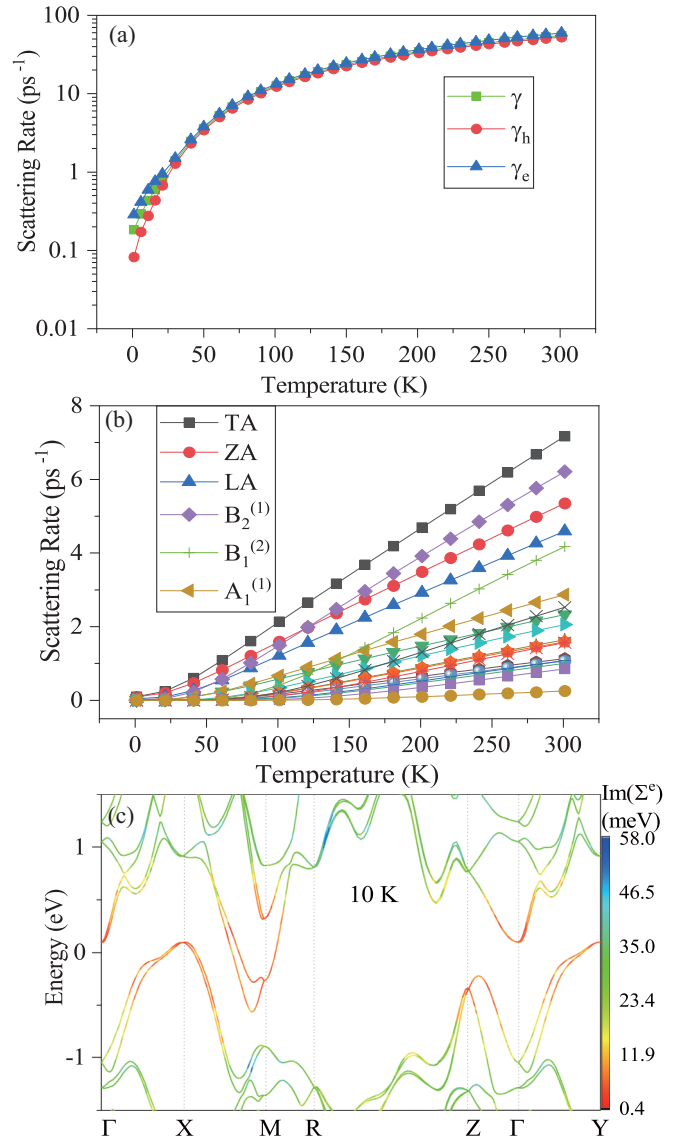


FIG. 4. (a) Temperature dependence of scattering rates for hole and electron carriers. The average scattering rates are also plotted. (b) Mode-resolved scattering rates versus the temperature. (c) Electron linewidth (in the unit of meV) along the k path for WP_2 at 10 K.

1528 $\text{cm}^2/\text{V s}$ for holes and electrons, respectively, by taking the scattering rates $\gamma_h = 0.67$ and $\gamma_e = 0.95$ ps^{-1} at 20 K and $m^* = 1.21m_0$ from the experiment [16]. Compared to the experimental mobilities [13], i.e., about 1830 $\text{cm}^2/\text{V s}$ for holes and 1270 $\text{cm}^2/\text{V s}$ for electrons at 20 K, our results are close to the experimental values. The carrier scattering mainly occurs to the Fermi pockets which have much less linewidth within the energy window of ± 0.5 eV, as shown in Fig. 4(c). This results in small scattering rates when carriers are scattered within the Fermi pockets.

As shown in Fig. 4(b), the mode-resolved scattering rates reveal that the acoustic modes play an important role in the carrier scattering. Among the phonon modes, the TA mode predominantly scatters carriers in the whole temperature range, followed by the modes of ZA and LA. It is found that the scattering rate of $B_2^{(1)}$ mode increases rapidly as the

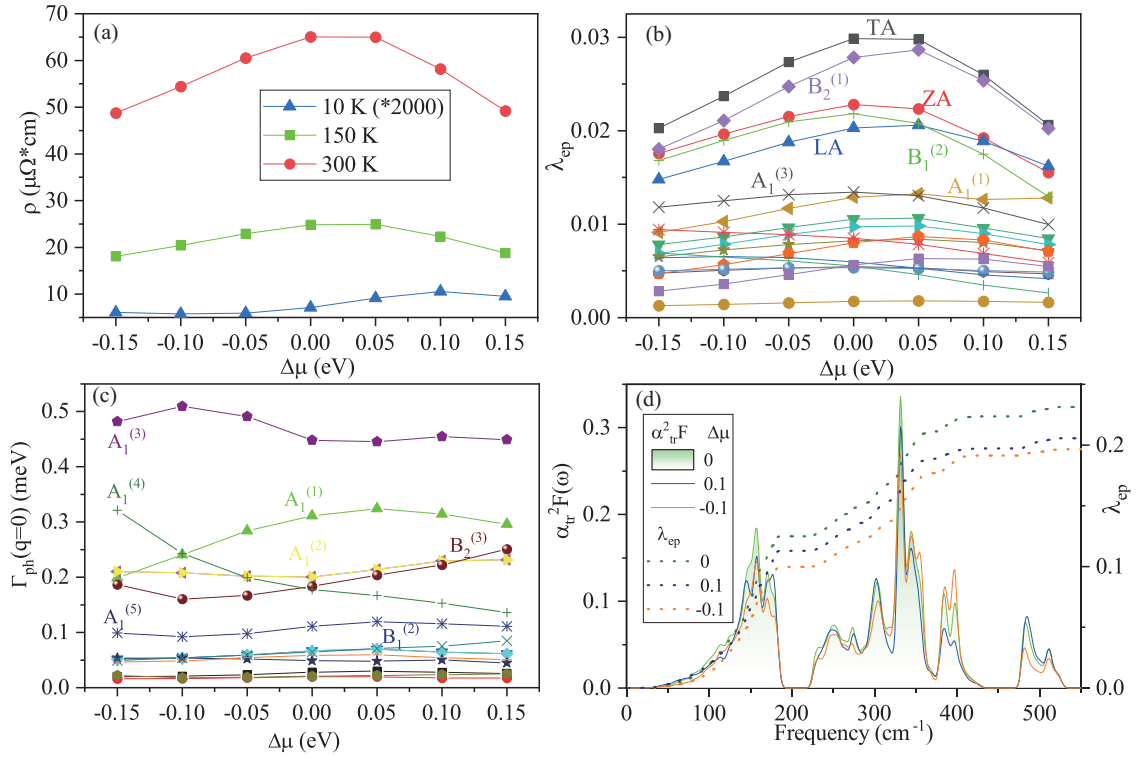


FIG. 5. (a) Chemical potential dependent resistivity at 10, 150, and 300 K. The resistivity at 10 K has been multiplied by 2000. (b) Mode-resolved EPC strength λ_{ep} as the function of chemical potential. (c) Mode-resolved phonon linewidth $\Gamma_{\text{ph}}(q = 0)$ as the function of chemical potential. (d) Frequency-dependent transport Eliashberg function $\alpha_{\text{tr}}^2 F(\omega)$ and integrated EPC strength λ_{ep} for $\Delta\mu = -0.1, 0$, and 0.1 eV.

temperature increases. For instance, at 140 K, the scattering rate of $B_2^{(1)}$ already exceeds the rate of the ZA mode. Similarly, the contribution of $B_1^{(2)}$ also increases rapidly as the temperature increases. At 300 K, the scattering rate of $B_1^{(2)}$ is close to that of the LA mode. The rapid increases of both $B_2^{(1)}$ and $B_1^{(2)}$ modes can account for the sharp decreases of resistivity ratio ρ_c/ρ_a at 100 K observed in the experiments [18]. According to the band structures in Fig. 1(c), the Fermi pocket along the path of Γ -X hosts the holes, which are more inclined to flow along the a axis than the c axis. As the temperature increases, the scattering enhancement of $B_2^{(1)}$ and $B_1^{(2)}$ significantly increases the resistivity along the a axis and thus decreases the resistivity ratio of ρ_c/ρ_a .

C. Chemical potential dependent resistivity

In semimetals and semiconductors, the carrier concentration as well as the Fermi level can be affected by impurity even with low concentration. For doped WP_2 , the shift of Fermi level makes the carrier uncompensated and hence changes the resistivity. Figure 5(a) shows the chemical potential dependent resistivity at three discrete temperatures. At 10 K, the resistivity is found to monotonously increase as the chemical potential increases from -0.1 to 0.1 eV. The ratio of $\Delta\rho(\mu = \varepsilon_F \pm 0.1)/\rho(\varepsilon_F)$ takes 67.6%, indicating a strong dependence on the chemical potential. At the temperatures 150 and 300 K, the resistivity is observed to decrease whenever the chemical potential deviates from pristine WP_2 . The maximum $\Delta\rho(\mu = \varepsilon_F \pm 0.1)/\rho(\varepsilon_F)$ only takes 17.8% and 16.3% at the temperatures 150 and 300 K, respectively. The behaviors of chemical

potential dependence of resistivity may come from the carrier scattering predominated by the phonon modes at different temperatures. For example, the acoustic modes dominate at the low temperatures while both the acoustic and optical modes heavily scatter the carriers at high temperatures.

As shown in Fig. 5(b), the mode-resolved EPC strength λ_{ep} is found to reach the maximum at the Fermi level for most phonon modes as the chemical potential increases. Generally, the low-frequency modes, especially the acoustic modes, have larger λ_{ep} than the high-frequency modes. Besides, the $B_2^{(1)}$ and $B_1^{(2)}$ modes are found to possess abnormal λ_{ep} , which is comparable to those of acoustic modes. Also, the modes of $A_1^{(1)}$ and $A_1^{(3)}$ possess considerably large λ_{ep} , which contributes to the carrier scattering at high temperatures. The different behaviors of $\rho(\Delta\mu)$ at low and high temperatures can be attributed to the carrier scattering of the optical modes, which are switched on at high temperatures.

Figure 5(c) shows the chemical potential dependent phonon linewidth at $\mathbf{q} = 0$. Compared to other modes, the A_1 group modes are found to possess larger linewidths and show strong dependence on the chemical potential. In contrast, the low-frequency modes $B_1^{(2)}$ and $B_2^{(1)}$, which have larger mode-resolved λ_{ep} , have much less phonon linewidths at $\mathbf{q} = 0$. The $A_1^{(1)}$ mode at the Fermi level has the linewidth of 0.32 meV, close to the experimental value of 0.36 meV. Also, the mode of $A_1^{(3)}$ is found to have larger linewidth than the modes of $A_1^{(4)}$ and $A_1^{(5)}$, in agreement with the experiment result [19,33]. As seen from Eq. (7), the phonon linewidth is proportional to the integral of $[f_{\mathbf{nk}}(T) - f_{\mathbf{nk}+\mathbf{q}}(T)]\delta(\varepsilon_{\mathbf{nk}+\mathbf{q}} -$

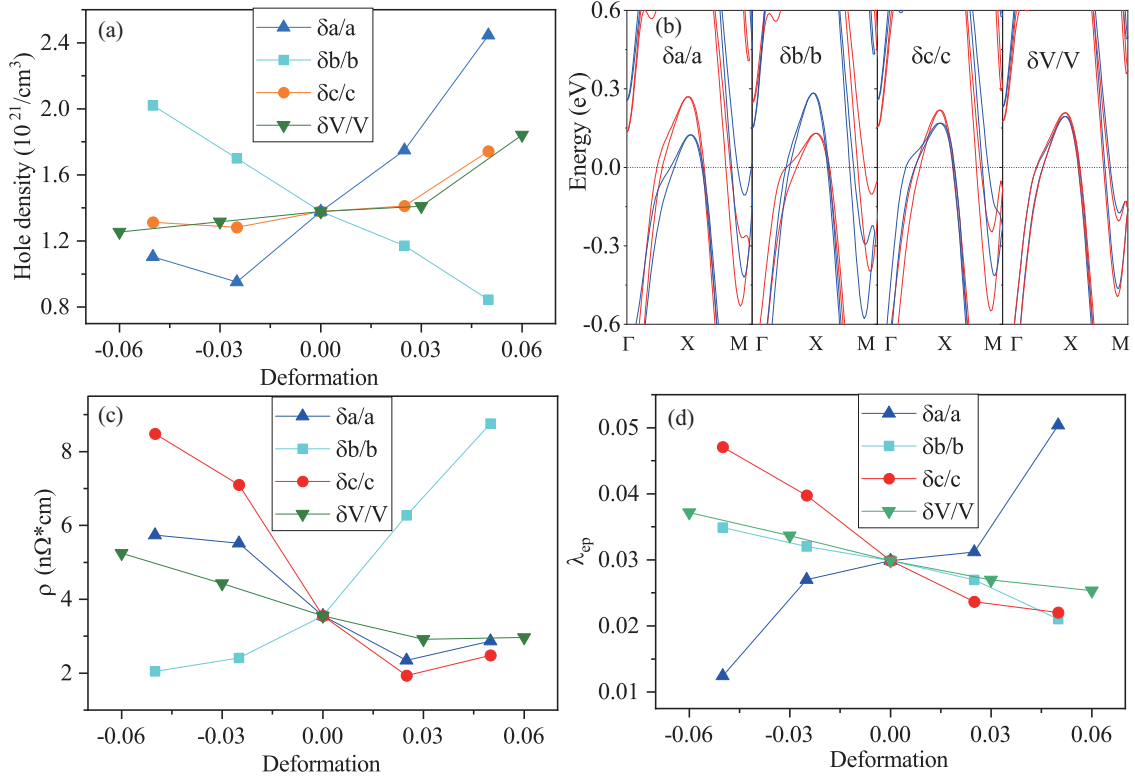


FIG. 6. (a) Hole density with respect to the uniaxial and volume strains. The uniaxial strain is applied along the a , b , and c axis, respectively, while the volume strain is applied with homogeneous volume deformation. (b) Electronic bands variation under the uniaxial ($\pm 2.5\%$) and volume ($\pm 3.0\%$) strains. The red and blue lines represent the bands with the tensile strain and the compressive strain, respectively. (c) The strain dependence of resistivity at 10 K. (d) The strain dependence of EPC strength for the TA mode.

$\varepsilon_{nk} - \omega_{qv}$), which is the difference of occupation probabilities between two states $|nk\rangle$ and $|mk + \mathbf{q}\rangle$. If $|\varepsilon_{m\mathbf{k}+\mathbf{q}} - \varepsilon_F|$, $|\varepsilon_{nk} - \varepsilon_F|$, and $\hbar\omega_{qv}$ are less than $k_B T$ (300 K), the phonon linewidth will reach maximum at room temperature. It means that the electrons are scattered within the energy windows of $k_B T$ (300 K) by absorbing a low-energy phonon. When the electrons are scattered far beyond the energy window of $k_B T$ (300 K) by absorbing a high-energy phonon, the phonon linewidth will show monotonous increasing with respect to the temperature. Since phonon energy of $A_1^{(1)}$ ($\hbar\omega = 21.3$ meV) is less than $k_B T$ (300 K), its phonon linewidth will inevitably reach the maximum at room temperature. For those modes of $A_1^{(3)}$ (42.9 meV), $A_1^{(4)}$ (47.2 meV), and $A_1^{(5)}$ (61.7 meV), a monotonous increase of phonon linewidth can be expected.

Figure 5(d) shows the transport Eliashberg function $\alpha_{\text{tr}}^2 F$ and the integrated EPC strength λ_{ep} with the chemical potential variations of -0.1 , 0 , and 0.1 eV. $\alpha_{\text{tr}}^2 F$ is found to have two gaps at 200 and 450 cm^{-1} , which correspond to the phonon band gaps. The peaks emerging at 170 and 330 cm^{-1} correspond to the modes of $B_2^{(1)}$ and $B_1^{(2)}$, which contribute to the resistivity at high temperatures. As the chemical potential deviates from the Fermi level, both the peaks are found to decrease, indicating the reduced contributions to the carrier scattering. Nevertheless, the spectrum below 80 cm^{-1} is found to increase as the chemical potential increases from -0.1 to 0.1 eV. Since the low-frequency modes contribute predominantly to the carrier scattering at low temperature, the resistivity will increase with increasing chemical potential.

The integrated EPC strength λ_{ep} takes 0.23 for WP₂, which is close to the strength of Au (0.22) but larger than Cu (0.14) and Ag (0.16) [34]. When the chemical potential changes by ± 0.1 eV, λ_{ep} decreases to 0.21 and 0.19, respectively.

D. Strain tuned carrier density and resistivity

Theoretically, the electronic transport of Weyl semimetals is predicted to be susceptible to lattice deformation due to the chiral anomaly of Weyl fermions in the Brillouin zone [36]. Experimentally, the resistivity is observed to decrease continuously, while the mobility and carrier density are enhanced for Weyl semimetal WTe₂ with increasing pressure [37]. Moreover, opposite behaviors of magnetoresistance have been observed when the strain is applied along the a and b axes of MoTe₂, respectively [38]. So far, the strain dependence of electronic transport has been seldom studied for WP₂. By using first-principles calculations and the Ziman resistivity formula, we calculate the strain effect on the electronic transport and carrier density of WP₂, as shown in Fig. 6. The uniaxial (volume) strain is defined as $\delta a/a$ ($\delta V/V$). Positive value means it is a tensile strain and vice versa. Our results reveal that the strain can effectively affect the carrier density in WP₂. However, the system still remains to be carrier compensated when the strain varies from -5% to 5% . The hole density generally increases when the tensile strain is applied along the a and c axes, while it decreases almost linearly when the tensile strain is along the b axis, as shown in Fig. 6(a). For the strain along the a axis, the hole density changes from

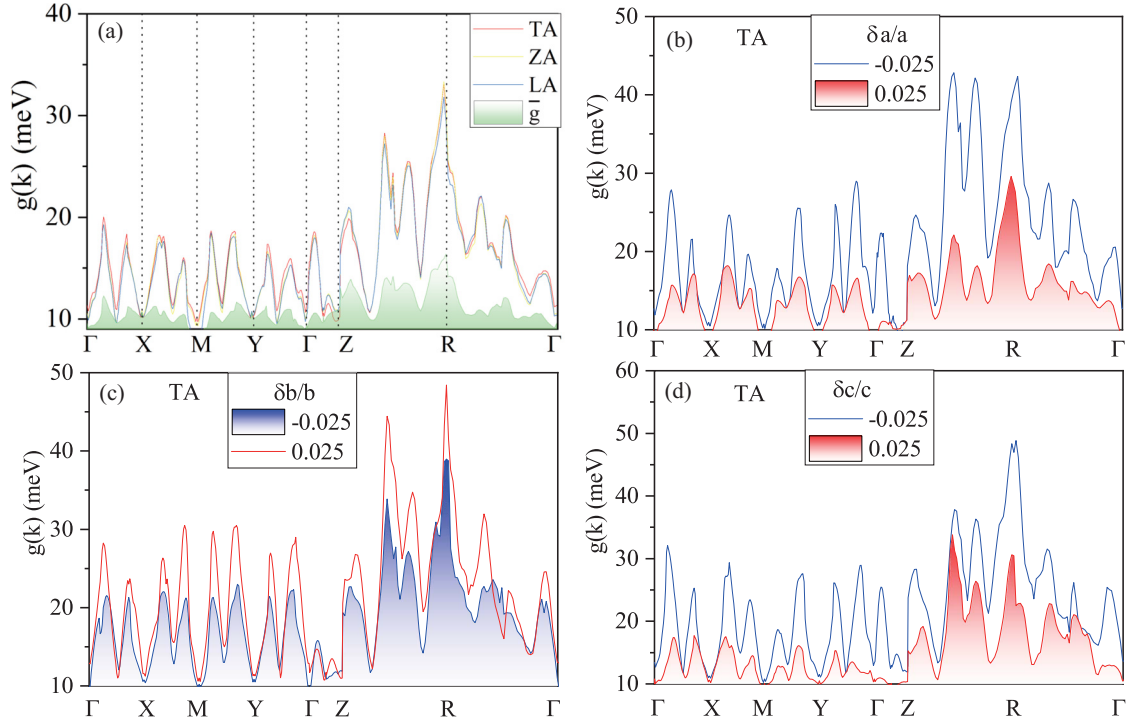


FIG. 7. (a) Mode-resolved EPC matrix elements for the LA, TA, and ZA mode along the k path in the Brillouin zone. The shaded green area represents the average value per mode. (b)–(d) The mode-resolved EPC matrix elements for the TA mode under the uniaxial strain along the a (b), b (c), and c (d) axis. The red (blue) curves represent the EPC matrix elements under tensile (compressive) strain.

–31% to 78% as the $\delta a/a$ increases, indicating a significant variation of carrier density tuned by strain. When the volume strain $\delta V/V$ increases from –6% to 6%, the hole density increases, different from the behavior of WTe_2 [37].

To explore the origin of carrier variation, we calculate the evolution of electronic bands near the Fermi level under the uniaxial and volume deformations, as shown in Fig. 6(b). When the tensile strain is applied along the a or c axes, the hole pocket shifts upwards, while the electron pocket moves downwards, leading to larger charge density. Similar Fermi pocket shifts are observed for WP_2 under the volume strain. In contrast, for the uniaxial strain along the b axis, the tensile strain results in the downward and upward shifts for the hole and electron pockets, respectively. This leads to the decrease of charge density with increasing deformation.

As shown in Fig. 6(c), the resistivity at 10 K is found to decrease under increasing uniaxial or volume strain, except the strain along the b axis. Usually, the tensile strain decreases the scattering potential $\partial V_{KS}/\partial u_{q\nu}$ and thus suppresses the EPC strength, which leads to the decrease of resistivity. Note that the resistivity also inversely depends on the density of states at the Fermi level. For WP_2 under the uniaxial strain along the b axis, the increase of resistivity can be attributed to the decrease of the density of states at the Fermi level due to the shifts of Fermi pockets. Since the TA mode predominantly contributes to the resistivity, we calculate the strain dependence of the EPC strength for the TA mode, as shown in Fig. 6(d). Increasing strain causes the EPC strengths to decrease except for the uniaxial strain along the a axis. The decrease of EPC strength can be attributed to the suppression of scattering potential due to the tensile strain. However, the

EPC strength is also inversely proportional to the frequency of phonon mode, which usually is softened under tensile strain. Therefore, the abnormal increase of EPC strength under the strain along the a axis can be attributed to the competition between the reduced scattering potential and phonon frequency.

Figure 7(a) shows the mode-resolved EPC matrix elements for the acoustic modes along the k path in the Brillouin zone. Since the transport properties are mainly contributed by the carriers from the Fermi pockets, we average the EPC matrix elements over the q mesh for the electronic bands within the energy window of ± 0.5 eV near the Fermi level. The EPC matrix elements oscillate greatly along the path in the Brillouin zone and the values of acoustic modes are about three times larger than the average. It is found that the value of the TA mode is slightly larger than those of ZA and LA modes. The EPC matrix elements are found to reach maximum at the R point. Since the TA mode predominately contributes to the electronic transport at low temperatures, we calculate the mode-resolved EPC matrix for the TA mode under different uniaxial strains, as shown in Figs. 7(b)–7(d). Compared with the case of compressive strain, the EPC matrix elements decrease largely when the tensile strains are applied along the a and c axes, which leads to the suppression of carrier scattering at low temperatures. In contrast, the tensile strain along the b axis brings about the enhancement of EPC matrix elements, which results in the enlargement of carrier scattering.

IV. CONCLUSION

We have investigated the electronic transport in the Weyl semimetal WP_2 by first-principles calculation plus the Ziman

resistivity formula. The calculated resistivity agrees well with the experimental results. Our results reveal that the acoustic modes, especially the TA mode, have large EPC strength and contribute predominantly to the resistivity at low temperatures. Carriers in the Fermi pockets have much less scattering rates than those outside the pockets. At low temperatures, holes are found to have significantly lower scattering rates than electrons. The scattering rates of $B_2^{(1)}$ and $B_1^{(2)}$ modes are found to increase rapidly as the temperature increases and contribute significantly to the resistivity at high temperatures. The low-temperature resistivity is found to increase monotonously with increasing chemical potential. In contrast, the resistivity at high temperatures shows nonmonotonous dependence on the chemical potential. Compared to other modes, the A_1 modes have larger phonon linewidths at $\mathbf{q} = 0$ and show significant dependence on the chemical potential. Moreover, both the carrier density and the resistivity can be well tuned by applying the strain to WP_2 . The tensile strains along the a and c axes bring about the increase of carrier density and hence the decrease of resistivity at low temperature, while the strain along the b axis leads to the opposite

behaviors of carrier density and resistivity. The strains induce the relative shifts of Fermi pockets as well as the variation of EPC matrix elements, which results in the variation of carrier density and resistivity. Our work casts some light on the nature of electronic transport properties driven by electron-phonon interaction for WP_2 . We hope that our study is helpful for future research on this material.

ACKNOWLEDGMENTS

This work is supported by the National Natural Science Foundation of China (Grants No. 11504027, No. 51961031, and No. 51541105) and the Foundation of Science and Technology Department of Liaoning Province (Grant No. 2019ZD0494). K.C.Z. acknowledges the fund support from Liaoning Revitalization Talents Program (Grant No. XLYC2007120). Y.L. acknowledges the support from the Science Foundation of Hebei Province (Grant No. A2015203021) and the Key Project of Hebei Educational Department, China (Grant No. ZD2018015).

-
- [1] N. P. Armitage, E. J. Mele, and A. Vishwanath, *Rev. Mod. Phys.* **90**, 015001 (2018).
- [2] B. Yan and C. Felser, *Annu. Rev. Condens. Matter Phys.* **8**, 337 (2017).
- [3] H. Zheng and M. Zahid Hasan, *Adv. Phys.: X* **3**, 1466661 (2018).
- [4] K. Das and A. Agarwal, *Phys. Rev. B* **100**, 085406 (2019).
- [5] C. Shekhar, A. K. Nayak, Y. Sun, M. Schmidt, M. Nicklas, I. Leermakers, U. Zeitler, Y. Skourski, J. Wosnitzer, Z. Liu, Y. Chen, W. Schnelle, H. Borrmann, Y. Grin, C. Felser, and B. Yan, *Nat. Phys.* **11**, 645 (2015).
- [6] W. Gao, N. Hao, F. W. Zheng, W. Ning, M. Wu, X. Zhu, G. Zheng, J. Zhang, J. Lu, H. Zhang, C. Xi, J. Yang, H. Du, P. Zhang, Y. Zhang, and M. Tian, *Phys. Rev. Lett.* **118**, 256601 (2017).
- [7] P. K. Tanwar, M. S. Alam, M. Ahmad, D. Kaczorowski, and M. Matusiak, *Phys. Rev. B* **106**, L041106 (2022).
- [8] F. C. Chen, X. Luo, J. Yan, Y. Sun, H. Y. Lv, W. J. Lu, C. Y. Xi, P. Tong, Z. G. Sheng, X. B. Zhu, W. H. Song, and Y. P. Sun, *Phys. Rev. B* **98**, 041114(R) (2018).
- [9] P. Li, C. Zhang, Y. Wen, L. Cheng, G. Nichols, D. G. Cory, G. X. Miao, and X. X. Zhang, *Phys. Rev. B* **100**, 205128 (2019).
- [10] G. Autes, D. Gresch, M. Troyer, A. A. Soluyanov, and O. V. Yazyev, *Phys. Rev. Lett.* **117**, 066402 (2016).
- [11] M.-Y. Yao, N. Xu, Q. S. Wu, G. Autes, N. Kumar, V. N. Strocov, N. C. Plumb, M. Radovic, O. V. Yazyev, C. Felser, J. Mesot, and M. Shi, *Phys. Rev. Lett.* **122**, 176402 (2019).
- [12] N. Kumar, Y. Sun, N. Xu, K. Manna, M. Yao, V. Suss, I. Leermakers, O. Young, T. Forster, M. Schmidt, H. Borrmann, B. Yan, U. Zeitler, M. Shi, C. Felser, and C. Shekhar, *Nat. Commun.* **8**, 1642 (2017).
- [13] A. Wang, D. Graf, Y. Liu, Q. Du, J. Zheng, H. Lei, and C. Petrovic, *Phys. Rev. B* **96**, 121107(R) (2017).
- [14] M. Simoncelli, N. Marzari, and A. Cepellotti, *Phys. Rev. X* **10**, 011019 (2020).
- [15] A. Cepellotti and N. Marzari, *Phys. Rev. X* **6**, 041013 (2016).
- [16] J. Gooth, F. Menges, N. Kumar, V. Säb, C. Shekhar, Y. Sun, U. Drechsler, R. Zierold, C. Felser, and B. Gotsmann, *Nat. Commun.* **9**, 4093 (2018).
- [17] J. Coulter, R. Sundararaman, and P. Narang, *Phys. Rev. B* **98**, 115130 (2018).
- [18] B. Su, Y. Song, Y. Hou, X. Chen, J. Zhao, Y. Ma, Y. Yang, J. Guo, J. Luo, and Z. G. Chen, *Adv. Mater.* **31**, 1903498 (2019).
- [19] G. B. Osterhoudt, Y. Wang, C. A. C. Garcia, V. M. Plisson, J. Gooth, C. Felser, P. Narang, and K. S. Burch, *Phys. Rev. X* **11**, 011017 (2021).
- [20] S. Ponce, W. Li, S. Reichardt, and F. Giustino, *Rep. Prog. Phys.* **83**, 036501 (2020).
- [21] P. B. Allen, *Phys. Rev. B* **13**, 1416 (1976).
- [22] F. J. Pinski, P. B. Allen, and W. H. Butler, *Phys. Rev. B* **23**, 5080 (1981).
- [23] S. Y. Savrasov and D. Y. Savrasov, *Phys. Rev. B* **54**, 16487 (1996).
- [24] F. Giustino, *Rev. Mod. Phys.* **89**, 015003 (2017).
- [25] S. Ponce, E. R. Margine, C. Verdi, and F. Giustino, *Comput. Phys. Commun.* **209**, 116 (2016).
- [26] A. A. Mostofi, J. R. Yates, Y.-S. Lee, I. Souza, D. Vanderbilt, and N. Marzari, *Comput. Phys. Commun.* **178**, 685 (2008).
- [27] P. Giannozzi, S. Baroni, N. Bonini, M. Calandra, R. Car, C. Cavazzoni, D. Ceresoli, G. L. Chiarotti, M. Cococcioni, I. Dabo, A. D. Corso, S. de Gironcoli, S. Fabris, G. Fratesi, R. Gebauer, U. Gerstmann, C. Gougoussis, A. Kokalj, M. Lazzeri, L. Martin-Samos, A. P. Seitsonen *et al.*, *J. Phys.: Condens. Matter* **21**, 395502 (2009).
- [28] D. R. Hamann, *Phys. Rev. B* **88**, 085117 (2013).
- [29] J. P. Perdew, K. Burke, and M. Ernzerhof, *Phys. Rev. Lett.* **77**, 3865 (1996).
- [30] M. van Setten, M. Giantomassi, E. Bousquet, M. Verstraete, D. Hamann, X. Gonze, and G.-M. Rignanese, *Comput. Phys. Commun.* **226**, 39 (2018).

- [31] X. C. Pan, Y. Pan, J. Jiang, H. Zuo, H. Liu, X. Chen, Z. Wei, S. Zhang, Z. Wang, X. Wan, Z. Yang, D. Feng, Z. Xia, L. Li, F. Song, B. Wang, Y. Zhang, and G. Wang, *Front. Phys.* **12**, 127203 (2017).
- [32] F. C. Chen, H. Y. Lv, X. Luo, W. J. Lu, Q. L. Pei, G. T. Lin, Y. Y. Han, X. B. Zhu, W. H. Song, and Y. P. Sun, *Phys. Rev. B* **94**, 235154 (2016).
- [33] D. Wulferding, P. Lemmens, F. Buscher, D. Schmeltzer, C. Felser, and C. Shekhar, *Phys. Rev. B* **102**, 075116 (2020).
- [34] A. Giri, M. V. Tokina, O. V. Prezhdo, and P. E. Hopkins, *Mater. Today Phys.* **12**, 100175 (2020).
- [35] W. Li, J. Carrete, N. A. Katcho, and N. Mingo, *Comput. Phys. Commun.* **185**, 1747 (2014).
- [36] D. I. Pikulin, A. Chen, and M. Franz, *Phys. Rev. X* **6**, 041021 (2016).
- [37] Y. Li, J. Liu, P. Zhang, J. Zhang, N. Xiao, L. Yu, and P. Niu, *J. Mater. Sci.* **55**, 14873 (2020).
- [38] J. Yang, J. Colen, J. Liu, M. C. Nguyen, G. Chern, and D. Louca, *Sci. Adv.* **3**, eaao4949 (2017).